Role of Surface Grafted Polymers on Mechanical Reinforcement of Metal-Organic Framework-Polymer Composites

Xiaozhou Yang,[a] Yongtao Hu,[a] Brittany L. Bonnett,[a] Sarah E. Blosch,[b] Hannah D. Cornell,[a] Bradley Gibbons,[a] Claudio Amaya Santos,[a] Stefan Ilic,[a] Amanda J. Morris[a,b]*

[a]Department of Chemistry, Virginia Tech, Blacksburg, VA 24060, United States

[b]Macromolecules Innovation Institute, Virginia Tech, Blacksburg, VA 24061, United States

Keywords: metal-organic frameworks, MOF-polymer composite, grafting-from, SI-ATRP, mechanical reinforcement, interface

ABSTRACT: Utilizing metal-organic frameworks (MOFs) as reinforcing fillers for polymer composite is a promising strategy thanks to the low density, high specific modulus, and tunable aspect ratio (AR). However, it has not been demonstrated for MOF-reinforced polymer composite using MOFs with high AR and polymer-grafted surface, both of which are extremely important factors for efficient load transfer and favorable particle-matrix interaction. Therefore, we designed a MOF-polymer composite system using high AR MOF PCN-222 as the mechanical reinforcer. Moreover, we developed a synthetic route to graft poly(methyl methacrylate) (PMMA) from the surface of PCN-222 through surface-initiated atomic transfer radical polymerization (SI-ATRP). The successful growth of PMMA on the surface of PCN-222

was confirmed via proton-nuclear magnetic resonance and infrared spectroscopy. Through thermogravimetric analysis, the grafting density was found to be 0.18 chains/nm^2. The grafted polymer molecular weight was controlled ranging from 50.3 to 158 kDa as suggested by size exclusion chromatography. Finally, we fabricated MOF-polymer composite films by doctor-blading technique and measured the mechanical properties through tension mode of dynamic mechanical analysis. We found that mechanical properties of the composites were improved with increasing grafted PMMA molecular weight. The maximum reinforcement, a 114% increase in Young's modulus at 0.5 wt% MOF loading in comparison to pristine PMMA films, was achieved when grafted molecular weight was higher than matrix molecular weight, which was in good agreement with previous literature. Moreover, our composite presents the highest reinforcement measured via Young's modulus at low weight loading among MOF-reinforced polymer composites due to the high MOF AR and enhanced interface. Our approach offers great potential for light-weight mechanical reinforcement with high AR MOFs and a generalizable grafting-from strategy for porphyrin-based MOFs.

INTRODUCTION

The development of metal-organic framework (MOF)-polymer composites has attracted enormous attention in the recent decade.[1-5] Such composite materials not only show the characteristic functions of MOF particles but also retain the flexibility and processibility of polymer matrix. For example, MOFs have been utilized to introduce size selective adsorption/separation of gases and solvents to traditional polymer membranes.[6-10] In order to expand the scope of MOF-polymer composites, various polymer preparation strategies, such as atomic layer deposition coated fibers,[11-17] mixed-matrix membrane,[18-21] and electrospun polymer fibers,[22-27] have been developed for fabrication of freestanding and transportable MOF-polymer composites.

One intriguing yet under-developed applications of MOF-polymer composites is mechanical reinforcement. Thanks to the high porosity, the density of MOFs is often one magnitude lower than

traditional reinforcers, making them exceptional reinforcing fillers for low-weight polymer composites. For example, MIL-53-NH_2 and PCN-222 have densities of 0.35 and 0.52 g/cm^3, respectively, whereas clay nanoparticles (1.50 g/cm^3), cellulose nanocrystals (1.5 g/cm^3), and carbon fibers (2.15 g/cm^3) all display significantly higher densities.[28-31] As a result of the low density, MOFs exhibit higher specific moduli (defined as modulus divided by density) when compared to those conventional fillers (e.g., 174-270 GPa·g^{-1}·cm^3 for MIL-53 and 145-165 GPa·g^{-1}·cm^3 for cellulose nanocrystals).[28, 32] Given such low density and high specific modulus, MOFs are able to provide sufficient mechanical reinforcement under a minimum weight loading, which can increase energy efficiency for several industrial applications such as aerospace and automotive engineering. Several studies have focused on MOF-reinforced polymer composites.[33-39] Our group previously used PCN-222 with high aspect ratios (AR, up to 54) and low density (0.52 g/cm^3) to enhance the mechanical properties of PMMA.[40] We have found that, at a very low weight percent loading of MOF (0.5 wt%), the Young's modulus was increased nearly two-fold in comparison to pristine PMMA. The reinforcing mechanism of the PCN-222/PMMA composites was consistent with a modified Halpin-Tsai model.

One major issue for particle-reinforced polymer composites results from the attractive van der Waals interaction that causes particle aggregation within the polymer matrix.[41] The poor interaction between the particle surface and polymer matrix significantly raises the energy barrier required to disperse the particles.[42] The lack of interaction at the particle-matrix interface also induces formation of air and solvent voids near particle surface, which can lead to decreases of interfacial friction, stress transfer, and thermomechanical properties such as T_g and stiffness.[43-45] To enhance the interfacial adhesion, polymers that are structurally similar or induce specific interactions (e.g., hydrogen bonding, electrostatic force) with the matrix polymer can be grafted on particle surface. With strategic control of graft molecular weight and grafting density, the matrix polymer chains can penetrate through the grafting chains to induce so-called "wet brush" regime, resulting in strengthened interface as well as improved particle dispersion and composite performance.[41] Hwang et al. showcased that PMMA-grafted multiwalled carbon nanotubes

could strongly bind to the matrix PMMA through polymer entanglement, resulting in improved load transfer process.[46] When the molecular weight of grafted polymers is equal to or greater than that of the matrix polymers, the matrix chains penetrate through the surface polymers, strengthening the interface and improving the stress transfer between matrix and filler.[42] Several groups have engineered the MOF surface with various polymers (e.g., poly(alkyl glycidyl ether) and polyimide) to investigate the effect of surface grafted polymer on the mechanical properties of MOF-polymer composites.[37, 39] However, MOFs with high AR are desired for ideal mechanical reinforcement. The abovementioned studies were limited by the low AR of the selected MOFs, potentially causing insufficient load transfer and reinforcement. Moreover, a thorough investigation into the development of optimized surface-grafted high AR MOF particle and its relationship with composite mechanical properties must be established.

In our previous endeavors, we systematically developed conditions to synthesize a low-density MOF PCN-222 (0.52 g/cm^3), which had the highest AR for non-templated MOFs to the best of our knowledge.[47] We also identified the effect of MOF AR on the mechanical properties of PCN-222-based MOF-polymer composites.[40] Therefore, in this work, we continue the investigation of the mechanical reinforcement of PCN-222 with a focus on tuning the interfacial properties by grafting PMMA from MOF surface. A three-step synthesis including surface-initiated atomic transfer polymerization (SI-ATRP) was designed to grow PMMA with controllable molecular weight on the surface of PCN-222. A series of thorough characterization techniques unveiled the properties of grafted PMMA and the relationship between grafted polymer and composite mechanical properties. As the molecular weight of polymer grafts approached or exceeded the molecular weight of matrix polymer, the MOF-polymer composite exhibited the best reinforcement. Our composite system was found to have one of the highest reinforcing performances at low weight percentage of MOF (0.5 wt%) for MOF-polymer composite to the best of our knowledge.

EXPERIMENTAL

Materials. All materials were purchased from commercial sources and used without purification except methyl methacrylate, which was purified by silica gel. Poly(methyl methacrylate) (PMMA, average M_w ~120,000), zirconium[30] oxychloride octahydrate ($ZrOCl_2 \cdot 8H_2O$, ≥99.5%), N, N, N′, N″, N″-pentamethyl diethylenetriamine (PMDETA, 99%), copper (I) bromide (CuBr, 98%), acetonitrile (≥99.9%), triethylamine (TEA, 99%), 4-aminobenzoic acid (ABA, 99%), and a-bromoisobutyryl bromide (BIBB, 98%) were purchased from Sigma-Aldrich (St. Louis, MO, USA). *meso*-Tetra(4-carboxyphenyl)porphyrin (TCPP, >97%) and difluoracetic acid (DFA, 98%) were acquired from Frontier Scientific (Logan, UT, USA) and Oakwood Chemical (Estill, SC, USA), respectively. Chloroform (≥99.9%) and *N,N*-dimethylformamide (DMF, ≥99.9%) were obtained from Fischer Scientific (Hampton, NH, USA). Myristic acid (>99.9%) was purchased from Tokyo Chemical Industry Co., LTD (Tokyo, Japan). Dimethylsulfoxide-d_6 (DMSO- d_6) was obtained from Cambridge Isotope Laboratories (Andover, MA, USA). Zinc nitrate hexahydrate ($Zn(NO_3)_2 \cdot 6H_2O$, 99%) was purchased from Alfa Aesar (Ward Hill, MA, USA).

PCN-222 synthesis. PCN-222 was synthesized *via* solvothermal synthesis following reported literature.[47] Typically, for the synthesis of P1 (PCN-222 with highest aspect ratio, AR = 48 ± 14), $ZrOCl_2 \cdot 8H_2O$ (151 mg), TCPP (15.8 mg), and DFA (2.07 mL) were charged in a 20 mL vial along with DMF (14 mL). Subsequently, TEA (2.2 μl) was added to the solution, which was sonicated for 2 mins and placed in a 120 °C oven for 48 hours. The purple powder was collected *via* centrifugation and washed with DMF and acetone three times. The air-dried PCN-222 particles were further activated in a vacuum oven at 60 °C overnight.

Synthesis of initiator [48]. The synthesis of initiator was modified from reported literature.[49] ABA (1.19 g) was dissolved in a round bottom flask filled with 60 mL anhydrous THF. After dissolution, $NaHCO_3$ (2.19 g) was added. In a separate beaker, BIBB (2 g) was dissolved in 10 mL THF, which was added to the septum-sealed flask through syringe. The flask was kept in an ice bath during BIBB addition. The mixture was then stirred at room temperature for 6 h. The resulting solution was acidified by adding few

drops of concentrated H_2SO_4 to pH~2. DCM (60 mL) and water (200 mL) were charged to the solution to extract Ini into the organic layer, which was isolated and further washed with water three times until ^{1}H-NMR shows no trace of starting materials. Finally, the organic solution was dried over Na_2SO_4 and further *via* rotary evaporation to give yellow powders. ^{1}H-NMR (500 MHz, DMSO-d_6): δ 12.70 (s, 1H), δ 10.04 (s, 1H), δ 7.90 (d, J=8.4 Hz, 2H), δ 7.80(d, J=8.4 Hz, 2H), δ 1.99 (s, 6H).

Postsynthetic modification with Ini to synthesize P1-Ini. In a typical experiment, PCN-222 (P1, 100 mg, 0.0417 mmol) was dispersed with 5 mM Ini solution in DMF (33.34 mL) in a 100 mL round bottom flask. The mixture was then stirred for 24 hours at 60 °C. To remove unreacted Ini, the P1-Ini powders were soaked in DMF at 100 °C overnight, followed by DMF wash three times. The final P1-Ini suspension was used for the next step of zinc metalation without drying. To measure the content of Ini loaded in MOF, P1-Ini was dispersed in DMSO-d_6 and digested by few drops of concentrated H_2SO_4 for ^{1}H-NMR.

Postsynthetic modification with $Zn(NO_3)_2{\cdot}6H_2O$ to yield P1-Ini-Zn. In the previously prepared P1-Ini suspension (0.0417 mmol P1), 10 equivalence of $Zn(NO_3)_2{\cdot}6H_2O$ (124 mg, 0.417 mmol) was charged. The mixture was stirred at 100 °C for 6 h. Then the suspension was washed with DMF and acetone three times each and soaked in acetone overnight before another three times of acetone wash. Lastly, the acetone-washed powders were dried in air and then a vacuum oven at 60 °C overnight.

Surface-initiated Atomic Transfer Radical Polymerization (SI-ATRP). For a typical reaction, P1-Ini-Zn (44 mg, 0.0184 mmol) was charged in a Schlenk tube, and vacuum was subsequently applied for 2 hours to evacuate air from the pores of the MOF. MMA (4.6 mL) and PMDETA (19.3 μL, 0.092 mmol) was then added to the Schlenk tube under nitrogen atmosphere. Notably, MMA was passed through a silica gel column before using to remove inhibitor, and MMA is served as both solvent and monomer (bulk polymerization) to yield high molecular weight. The mixture underwent four cycles of freeze-pump-thaw with liquid nitrogen. After the last thawing process, the tube was transferred to an argon-filled glove box. Pre-evacuated dry CuBr powders (13.2 mg, 0.092 mmol) were measured in the glove box and added

to the Schlenk tube. The final mixture was stirred for 1-6 hours at 65 °C. The molar ratio of P1-Ini-Zn:CuBr:PMDETA was weighed to be 1:5:5. After polymerization, the P1-g-PMMA particles were isolated *via* centrifugation and washed with acetonitrile three times. To further remove residual CuBr, the particles underwent Soxhlet solvent exchange for three days. The resulting particles were dried in a 60 °C vacuum oven overnight to give the final product.

Powder X-ray Diffraction. PXRD was collected on a Rigaku Miniflex diffractometer (Cu Kα radiation λ = 1.5418 Å). Data was obtained over 2θ = 2−50° at a 0.05° resolution and a 1.0°/min scanning rate.

MOF digestion and ^{1}H-NMR Spectroscopy. In general, MOF particles (~5 mg) was dispersed in DMSO-d_6 (600 μL) in a 2-dram scintillation vial and digested by adding few drops of concentrated H_2SO_4. The suspension was sonicated and heated at 85 °C for 30 mins until particles decomposed. ^{1}H-NMR was collected on an Agilent U4-DD2 400 MHz NMR spectrometer.

Preparation of MOF-Polymer Composite Films. The detailed procedure can be found in our previous publication. In brief, MOF particles (2.5 mg) were dispersed in chloroform, followed by 5 min sonication. PMMA (0.5 g) was then added to the suspension, which was sonicated for another min and stirred at room temperature overnight. The resulting slurry was carefully poured onto a glass slide and casted by a doctor blade to give a homogeneous film. The film was then dried in air for 6 h and annealed in an oven at 120 °C overnight. Finally, the composite film was detached by soaking in water.

Scanning Electron Microscopy. MOF particles were dispersed in acetone and drop-casted on a silicon wafer for SEM analysis. All SEM samples were sputtered with a 4 nm thick Pt/Pd layer to increase conductivity. SEM were conducted with a LEO 1550 field-emission scanning electron microscope (Car Zeiss, Oberkochen, Germany) at 5.0 kV and a 10 mm working distance.

Thermogravimetric Analysis (TGA). TGA measurement was performed on a Q500 thermal analyzer (TA Instruments, New Castle, DE, USA). The MOF particles (~5 mg) were activated at 120 °C on a

Schlenk line overnight to ensure the removal of solvent prior to TGA. In a typical TGA experiment, samples were heated from 30 °C to 750 °C at a 10 °C/min rate under air.

BET Gas Adsorption. Gas adsorption behavior, surface area, and pore size were studied by a 3Flex surface analyzer (Micromeritics, Norcross, GA, USA) at 77 K. MOF particles (~30 mg) was charged into a Micromeritics sample cell, which was activated at 120 °C for 24 h.

Size Exclusion Chromatography (SEC). SEC was conducted on two MIXED-B Agilent PLgel 10 μm columns connected with a Wyatt Optilab rEX refractive index detector and a Wyatt Dawn Heleos 2 multi-angle light scattering detector. The dn/dc value used for PMMA was 0.087.[50] The flow rate was set at 1 mL/min. To prepare the sample, P1-g-PMMA (>10 mg) was digested by 1 M aqueous NaOH (3 mL) for 1 min under sonication. Ethyl acetate (5 mL) was then added to extract PMMA into the organic phase. After stirring the mixture at room temperature overnight, the organic layer was isolated and dried to give a thin layer of solid containing recovered PMMA. Finally, the product was dissolved in THF (1 mL) containing 0.025 wt % butylated hydroxytoluene before injecting to SEC.

Determination of Zn-TCPP *via* UV-Vis-NIR Spectroscopy. A digested P1-Ini-Zn aqueous solution was prepared to study the success of zinc metalation *via* UV-Vis spectroscopy. P1-Ini-Zn was digested by 1 M aqueous NaOH solution (~2 mL). The suspension was filtrated and scanned by a Cary 5000 UV-Vis-NIR Spectrophotometer (Agilent, Santa Clara, CA, USA).

Dynamic Mechanical Analysis (DMA). Details of measurement can be found in our previous publication.[40] In short, tensile tests were performed *via* the tension mode of DMA Q800 (TA Instruments, New Castle, DE, USA). Composite films were mounted on DMA clamps with “Controlled Force” mode at a 3 N/min ramp rate at 30 °C. The preload force was set to 0.02 N while the target force being 18 N.

Postsynthetic Modification of PCN-222 with Myristic Acid (MA). A solution of 1 M MA in DMF was prepared. Different amount of PCN-222 (2392.9 g/mol) was added to reach 10:1 stoichiometric ratio of MA to TCPP. The mixture was kept at 60 °C overnight under stirring.

RESULTS AND DISCUSSION

Synthesized *via* a modulated solvothermal reaction, PCN-222 is composed of 8-connected Zr_6 oxo clusters bound to carboxylic acids on TCPP, forming 37 Å channels along the c-axis surrounded by 13 Å micropores (**Figure 1b-inset**). To control the AR of PCN-222, a monocarboxylic acid (difluoracetic acid, DFA) was used as a modulator to hinder the growth of the (100) and (010) facets by competitively binding to the medal nodes. High AR MOF particles were attained (48 ± 14) as revealed by SEM (**Figure 1a**). Compared with the simulated PXRD pattern of PCN-222, the experimental PXRD indicated retained crystallinity and phase purity of the as-synthesized PCN-222 (**Figure 1b**). To simplify the nomenclature throughout this paper, PCN-222 with AR of 48 ± 14 will be referred as P1.

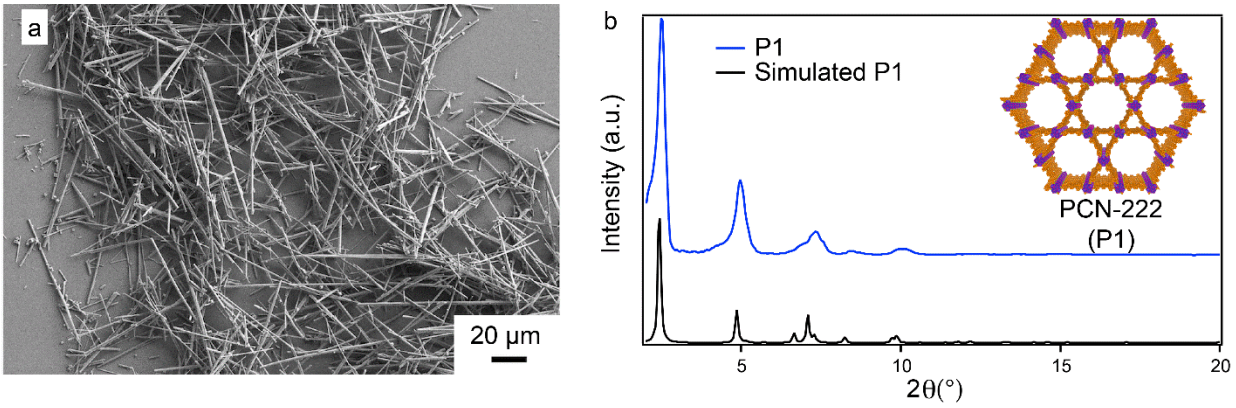

Figure 1. (a) SEM image of PCN-222 (P1). (b) PXRD patterns of as made P1 (blue) and simulated PCN-222 (black). Inset: schematic illustration of the crystal structure of P1 viewing along the c-axis. (orange = carbon, dark blue = Zirconium node, green = oxygen)

To graft polymers onto a particle surface, two primary strategies have been developed: grafting-to [51] and grafting-from [52]. The former designs and synthesizes polymers that contain one functional end group, which is capable of covalently bonding to the particle surface. Since the graft polymer is pre-synthesized, it is easier to control and characterize its properties, resulting in a more homogenous coating. However, the steric hindrance of polymer chains greatly prohibits the attachment of polymer and the interaction between functional end group and particle surface, resulting in low grafting molecular weight and grafting

density. On the other hand, grafting-from grows the polymer *in situ* from the particle surface through surface-anchored initiator. The negligible volume of monomers and catalysts prevents steric hindrance, giving rise to high graft molecular weight (>100 kDa) and grafting density (> 0.3 chains/nm^2).[52] Therefore, to attain better grafting outcomes, the grafting-from strategy was chosen to grow PMMA on the surface of PCN-222. Among a variety of surface-initiated controlled radical polymerization methods, surface-initiated atomic transfer radical polymerization (SI-ATRP) was selected because of its facile operation, mild reaction condition, and good compatibility with PMMA.

A three-step process was developed to facilitate the SI-ATRP of PMMA onto PCN-222. (**Scheme 1**). In the initial step, the as-synthesized pristine PCN-222 (P1) is incorporated with pre-made polymerization initiator [48], which can bind to the metal clusters through the carboxylates. (**Scheme 1a**) Then, metalation of the porphyrin linker of is required (Scheme 1b) because the incorporated MOF porphyrins are capable of binding the Cu^+ from the ATRP catalyst and attenuate its catalytic polymerization activity. Thus, it is necessary to perform porphyrin metalation (Zn^{2+} was used in this case) prior to ATRP. Finally, a classic ST-ATRP is carried out. (**Scheme 1c**)

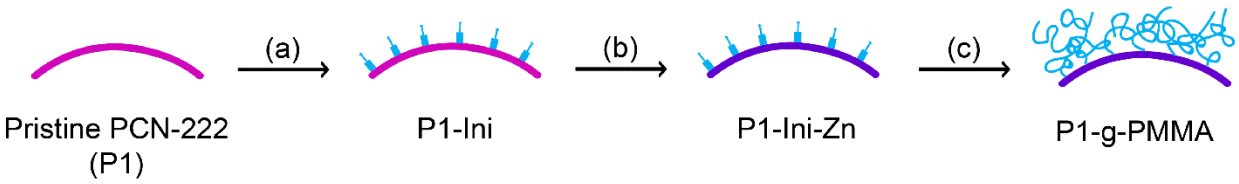

Scheme 1. The three-step process to graft PMMA from PCN-222 surface. (a) Postsynthetic modification of pristine P1 with initiator [48]. (b) Metalation of P1-Ini with Zn^{2+} so that the porphyrin of TCPP linker does not capture the Cu^+ catalyst used in SI-ATRP. (c) Grafting-from strategy to polymerize PMMA from MOF surface *via* SI-ATRP mechanism.

Initiator (Ini), 4-(2-bromo-2-methylpropanamido)benzoic acid, was prepared from amidization of 4-aminobenzoic acid and a commonly used ATRP initiator BIBB. Details of synthesis of Ini can be found in experimental section. Confirmation of successful Ini preparation was determined via ^{1}H NMR and mass

spectroscopy. (Figure S1) PSM of pre-formed P1 particles with Ini (termed P1-Ini) was performed in a DMF solution of Ini at 60 °C. To characterize Ini loading, the ratio of Ini to TCPP was measured by ^{1}H-NMR on MOF digested with concentrated H_2SO_4 (Figure S2). Comparison of the peak integration of protons on the TCPP and Ini revealed a nearly one to one molar ratio of the two components. Since a crystal unit cell of PCN-222 has one metal node and two TCPP linker based on the chemical formula $Zr_6(\mu_3\text{-}O)_8(OH)_8(TCPP)_2$, each metal node of P1-Ini is functionalized with two Ini molecules. Such high loading of Ini in MOF ensured an efficient polymerization initiation process and a high grafting density.

After functionalizing P1 with Ini, it is necessary to inhibit the metal capture ability of TCPP linker as discussed above (Figure S3). In fact, our initial trials with free-base TCPP all resulted in failed ATRP. Therefore, a zinc salt ($Zn(NO_3)_2{\cdot}6H_2O$) was selected to metalate the ligand since Zn^{2+} and Cu^{+} have similar size and affinity to the porphyrin.[53] Zn^{2+} metalated P1-Ini (P1-Ini-Zn) was confirmed by UV-Vis spectroscopy (Figure S4a). The electronic absorption spectra of porphyrins are highly sensitive to metalation as metal insertion changes the symmetry of the porphyrin and thus, the energetic position and intensity of observed transitions.[48, 54-55] Comparison of the spectra for P1-Ini and P1-Ini-Zn confirm metalation as the four Q-band absorption peaks of free-base TCPP from 500 to 680 nm merge to the expected two Q-bands bands for Zn-TCPP (540-630 nm). The experimental PXRD pattern of P1-Ini-Zn matched well with the simulated pattern of PCN-222 and previously measured P1-Ini, ensuring the crystal structure was maintained after PSM with Ini and Zn^{2+} metalation. (**Figure 2a**) Furthermore, the treatments did not cause significant damage to the MOF morphology, as the SEM revealed only a modest decrease in the average AR for P1-Ini-Zn (41 $\pm$ 12) compared to pristine P1 (AR 48 $\pm$ 14) (**Figure 2b**). ^{1}H-NMR of the H_2SO_4-degraded P1-Ini-Zn showed that initiator concentration remained nearly identical in the MOF after Zn^{2+} treatment (Figure S4b and S4c). Notably, the order of P1 modification, i.e., PSM with Ini or metalation with Zn^{2+} was interchangeable. The ^{1}H-NMR spectrum of digested P1-Ini-Zn and P1-Zn-Ini revealed an almost identical Ini to linker ratio (Figure S4) and the PXRD patterns of P1-Zn-Ini also resembled the simulated pattern (**Figure 2a**).

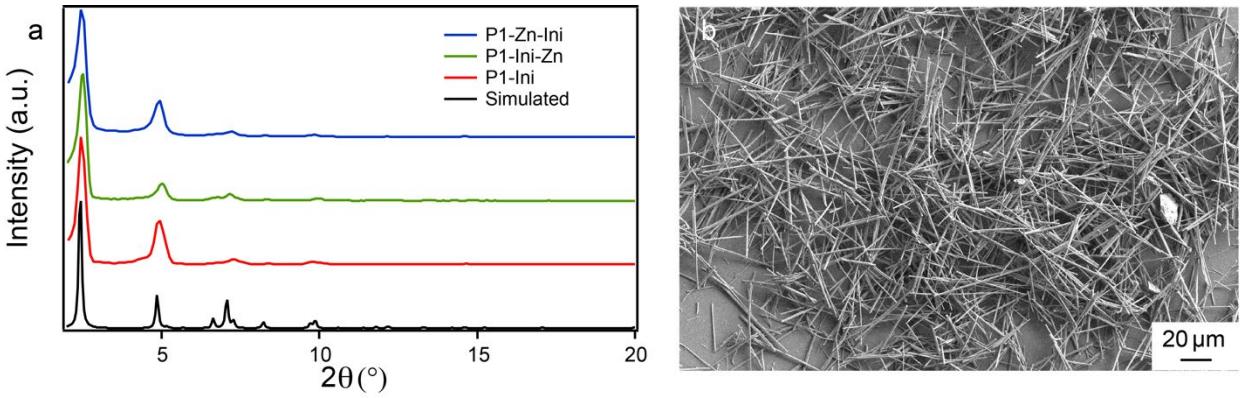

Figure 2. (a) Experimental PXRD pattern of P1-Ini (red), P1-Ini-Zn (green), P1-Zn-Ini (blue) and simulated pattern of PCN-222 (black). (b) SEM image of P1-Ini-Zn.

To graft PMMA from the surface of P1, SI-ATRP was chosen as the polymerization mechanism because of its facile operation, control of molecular weight, and wide range of suitable monomers.[56]For our ATRP approach, CuBr and PMDETA, respectively, served as catalyst and ligand, while monomer MMA was both the reagent and solvent since bulk polymerization tends to yield high molecular weight (**Figure 3a**). [57-58] The rod-like morphology of MOF particles remained consistent after ATRP process as revealed by SEM, however, the particles became shorter after polymerization and AR decreased from 41 ± 12 to 27 ± 7 (**Figure 3b**). The change was attributed to particle breakage from the rapid mechanical stirring required for polymerization. To prove the effect of mechanical agitation, P1-Ini-Zn was dispersed and stirred in the same condition as polymerization solution in the absence of freeze-pump-thaw (i.e., no removal of oxygen and no polymerization). The AR of resulting MOF decreased to 26 ± 3, similar to P1-g-PMMA (Figure S5 and Table S2). We also hypothesized that the growth of polymer inside the MOF pores, although greatly prohibited by the limited monomer diffusion within the MOF, could also contribute to particle breakage. Nonetheless, the PXRD of P1-g-PMMA confirmed that the crystal structure of PCN-222 was retained after polymerization (**Figure 3c**). Infrared spectra (IR) were acquired to confirm the presence of PMMA (**Figure 3d**). Compared with reference PMMA and MMA samples, the characteristic carbonyl stretch (C=O) corresponding to the methacrylate group of PMMA was observed at 1720 cm^{-1} in the spectrum of P1-g-PMMA (PMMA-grafted P1, highlighted in purple). The absence of

alkene (C=C) absorption peak at 1640 cm^{-1} in P1-g-PMMA sample (highlighted in blue) proved that the observed carbonyl group was originating solely from the PMMA and not MMA monomer.

To understand the nature of the grafted PMMA and determine if it was coordinatively bound to or physically adsorbed onto the MOF, we first ensured all the free-floating polymers and monomers were removed from the MOF by washing as-synthesized P1-g-PMMA three times with acetonitrile and then conducting Soxhlet solvent extraction with acetonitrile for three days. P1-g-PMMA was then soaked again in acetonitrile overnight, and the supernatant of the solution was collected for ^{1}H-NMR (**Figure 3e-i**). PMMA was not detected in the supernatant, which only showed residual solvent peaks (water, 3.29 ppm; acetonitrile, 2.07 ppm; and acetone, 2.09 ppm) (**Figure 3e-i**). As a reference, commercially available PMMA displayed a characteristic peak of methoxy protons at 3.56 ppm (highlighted in green) and peaks of methyl group at 0.58-1.06 ppm (highlighted in yellow) (**Figure 3e-iii**). We also collected ^{1}H-NMR spectrum on digested P1-g-PMMA by adding a few drops of conc. H_2SO_4 in DMSO-d_6 with 10 mg of MOF which was then passed through a 200 nm filter before collecting NMR data to remove MOF debris and improve the NMR signal. The proton peak positions of digested P1-g-PMMA clearly matched with the characteristic PMMA signals (**Figure 3e-ii**). The ^{1}H-NMR results further proved the growth of PMMA, which was coordinatively anchored on the MOF instead of physiosorbed.

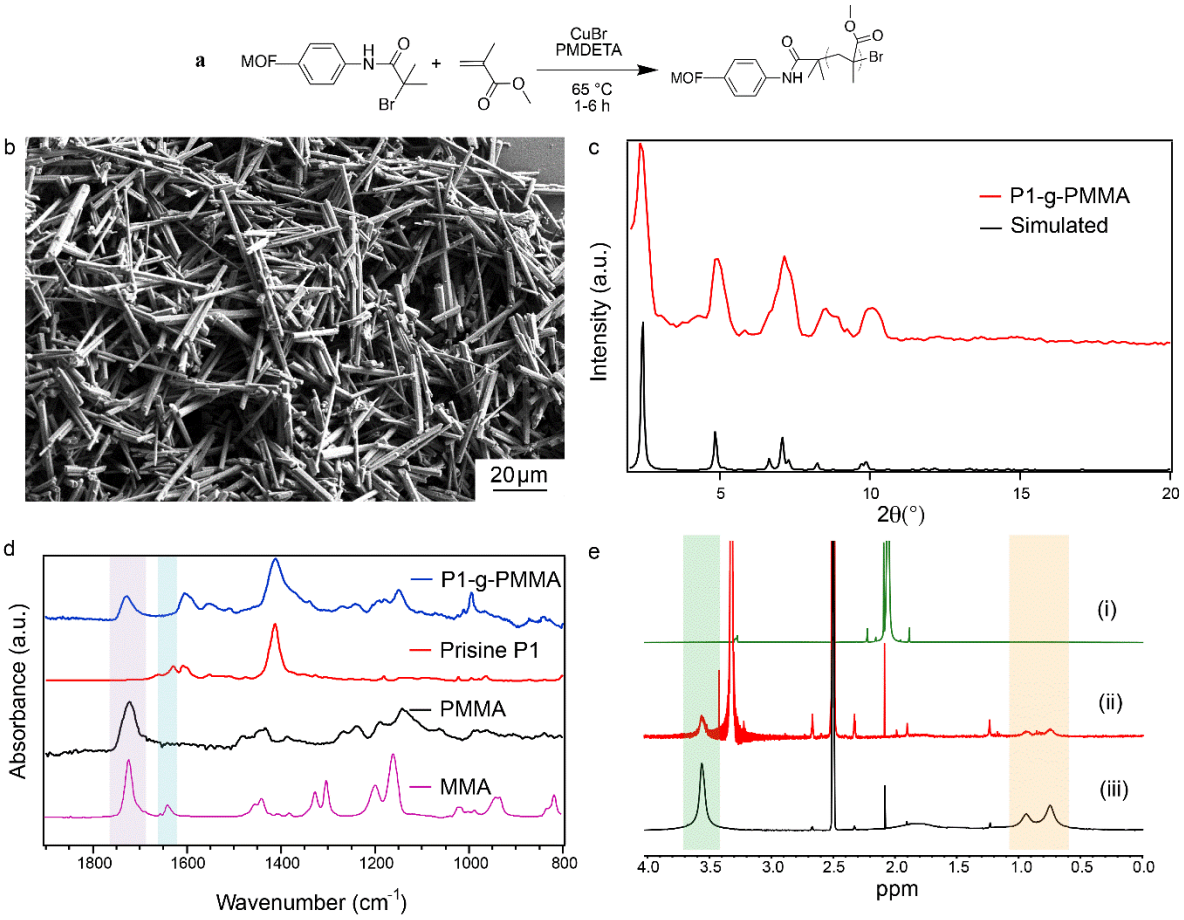

Figure 3. (a) Reaction scheme of SI-ATRP. (b) SEM image of P1-g-PMMA. (c) PXRD pattern of P1-g-PMMA and simulated PCN-222. (d) IR spectra of monomer (MMA), polymer (PMMA), pristine MOF (P1), and PMMA-grafted MOF (P1-g-PMMA). (e) ^{1}H-NMR spectra of (i) supernatant of acetonitrile-soaked P1-g-PMMA, (ii) acid-digested P1-g-PMMA dissolved in DMSO-d_6, and (iii) reference PMMA.

The effect of SI-ATRP on pore environment was probed by BET N_2 adsorption and desorption measurements (**Figure 4**). All three samples exhibited type IV N_2 sorption isotherm, typical of PCN-222. The BET surface area for pristine P1 and P1-Ini-Zn was calculated to be 1640 and 1572 m^2/g, respectively, which were comparable with literature values.[59] The slight decrease of BET surface area for P1-Ini-Zn was attributed to the incorporation of initiator and metalation of porphyrin. However, the attachment of initiator on metal nodes would only induce a subtle change in pore size and the pore width of porphyrin (~4 Å) is also below the limit of BET detection (~ 4.8 Å). Therefore, such variation in pore environment was not reflected on pore width distribution (**Figure 4b**). After grafting with polymer, the

BET surface area drastically decreased to 301 m^2/g. Since the inner MOFs were also decorated with Ini, it was reasonable to consider the possibility of polymer growing inside the MOF pores and causing the low surface area. To examine this concern, the pore environment of the MOF before and after polymerization was carefully investigated (**Figure 4b**). The pore size distribution of P1-g-PMMA was nearly identical to the two precursors, except for the loss of small micropores around 6 Å. The preserved pore environment (i.e., pore size distribution) after polymerization suggests that the polymerization did not occur at the inner pores of the MOF. Otherwise, we would observe certain degree of decrease of pore width. Therefore, the decrease of surface area from 1572 to 301 m^2/g indicates that the pore apertures on the surface of MOF were blocked by grafted high molecular weight PMMA, limiting N_2 access to the interior of the MOF and resulting in decreased observed specific surface area.

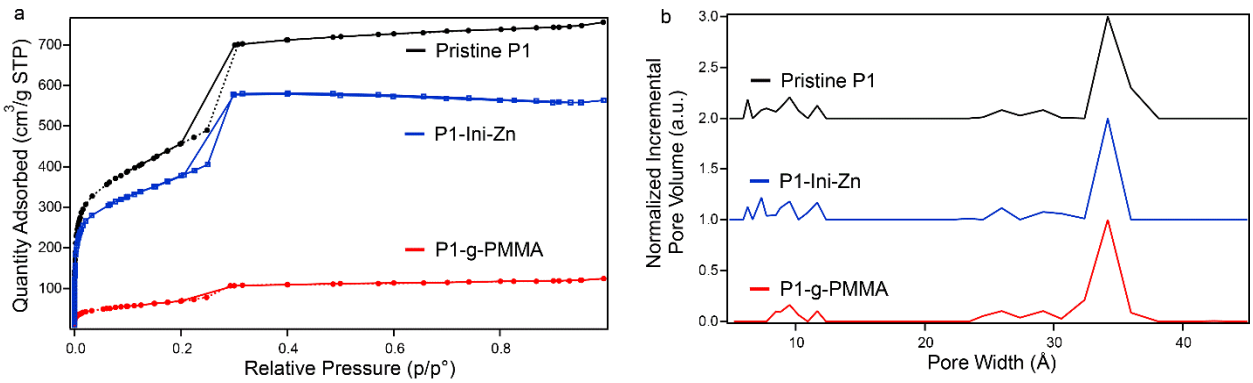

Figure 4. (a) N_2 adsorption and desorption isotherm of pristine P1, P1-Ini-Zn, and P1-g-PMMA. (b) Normalized incremental pore volume of pristine P1, P1-Ini-Zn, and P1-g-PMMA.

TGA was used to characterize the weight percentage and therefore, grafting density of PMMA on PCN-222 (**Figure 5**). A typical TGA curve of MOF sample conducted in air consists of 1) removal of residual solvent between 100-200 °C, 2) dehydroxylation of zirconium nodes at 300 °C, and 3) decomposition of TCPP ligands starting at 440 °C. Pristine P1 and P1-Ini-Zn showed similar weight loss behaviors, but P1-Ini-Zn exhibit a lower on-set degradation temperature (~410 °C) due to the incorporation of initiator. The final weight plateau of pristine P1 and P1-Ini-Zn after 600 °C was due to the remaining ZrO_x formed by oxidation of Zr node. On the other hand, reference PMMA started to degrade at 240 °C and continued

until 420 °C. During the oxidation process, pristine polymer was completely converted to CO_2, resulting in nearly 0% residual weight upon completion of the temperature ramp. P1-g-PMMA showed decomposition at 240 °C due to the degradation of PMMA. The difference of final residual weight of P1-Ini-Zn and P1-g-PMMA was calculated to be 13.6%, which was attributed to the weight percentage of grafted polymer. The grafting density σ (chains/nm^2) was calculated using the mass and molecular weight of polymer, as well as the density and volume of MOF:

$$\sigma = \frac{m_{polymer} \cdot N_A}{M_{polymer} \cdot SA} = \frac{m_{polymer} \cdot N_A}{M_{polymer} \cdot sa \cdot \frac{m_{MOF,total}}{\rho_{MOF} \cdot v_{MOF}}} \quad \text{Eq. 1}$$

where $m_{polymer}$ stands for the mass of the grafted polymer, $M_{polymer}$ represents the molecular weight of polymer determined by SEC, SA and sa refer to surface area of all the MOF particles and one single MOF particle, respectively. In short, $\frac{m_{polymer}}{M_{polymer}}$ yields the total number of polymer chains in mol, which was multiplied by Avogadro constant to convert to number of chains. The total number of polymer chains was divided by the accumulated external surface area of all the MOF particles to give number of chains per unit area. The grafting density σ of P1-g-PMMA was calculated to be 0.18 chains/nm^2. Given the density of surface nodes (0.338 nodes/nm^2) for PCN-222 (calculation details in SI, Figure S6), dividing grafting density by node density revealed that 53.3% of surface nodes were grafted with polymers. Comparing with grafting strategies for conventional particles (e.g., silica nanoparticles), our grafting density was higher than most of grafting-to approach (0.01-0.10 chains/nm^2) but lower than a typical grafting-from strategy (> 0.70 chains/nm^2).[42] Unlike these traditional materials (e.g., SiO_2 or metal nanoparticles), the surface of MOF is highly porous and therefore, available surface sites for anchoring initiator and grow polymers are limited, resulting in a relatively low grafting density. In addition, a portion of surface metal nodes were inevitably capped by linkers or modulators, which further decreased available sites for polymer grafts. Despite the lower grafting density in MOFs comparted to SiO_2, Kumar and Maillard et al. previously demonstrated significant mechanical reinforcement by well-dispersed particles with grafting densities of 0.10 chains/nm^2 or above.[60]

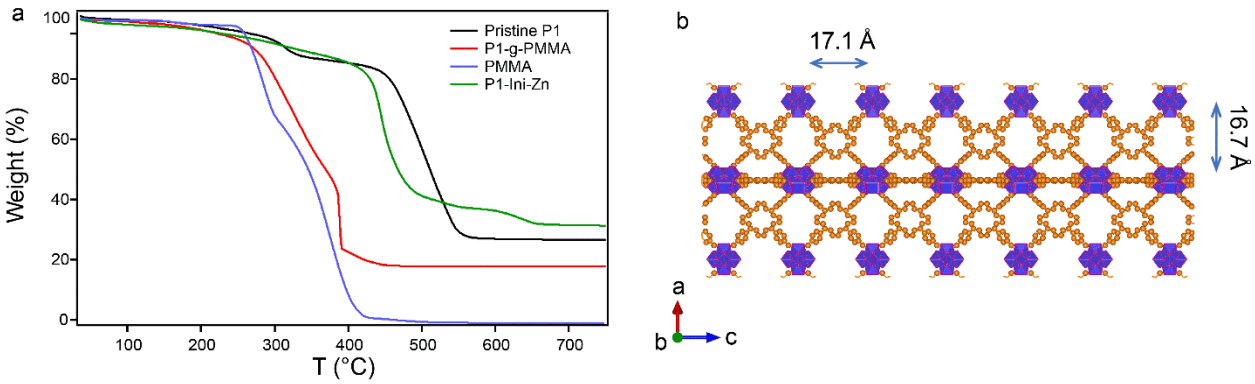

Figure 5. (a) TGA traces of pristine P1, P1-Ini-Zn, P1-g-PMMA, and reference PMMA. (b) Schematic illustration for determining dimensions of PCN-222.

Upon successfully grafting PMMA on the surface of MOF, it was important to demonstrate the control of polymer molecular weight, which could govern the mechanical reinforcing behaviors. By simply varying the polymerization time from 1 h to 6 h, we were able to obtain different molecular weights of the PMMA grafted to the MOF particles as evidenced by SEC (**Figure 6a**). To prepare SEC samples, P1-g-PMMA was digested with NaOH solution and the isolated PMMA was extracted by THF. Regarding the stability of PMMA under the basic digestion condition, we conducted same treatment on commercially available PMMA (120 kDa). The ^{1}H-NMR spectrum of 1M NaOH treated PMMA showed no additional peak in comparison to pristine polymer, ensuring the preserved PMMA structure (Figure S7). For P1-g-PMMA, SEC traces of recovered PMMA showed a decreasing retention time as reaction time increases, indicating the increased molecular weight as polymerization time increased (**Figure 6a**). The molecular weight and polydispersity (Đ) were summarized in **Table 1**. The linear growth of M_n as a function of monomer conversion indicated a typical controlled living polymerization system (**Figure 6b**). In addition, by plotting the natural log of initial monomer concentration divided by final monomer concentration versus reaction time, we were able to visualize the rate of the polymerization process (**Figure 6b**). At the beginning of polymerization (0 h, 1h, and 3 h), $\ln([M_0]/[M_t])$ vs. t followed a linear relationship, indicating a first order reaction.[61-62] But when molecular weight increased to 158 kDa at 6 h, the trend deviated from the linear trend and the polymerization slowed down. To explain the polymerization

kinetics, it is necessary to understand the chain dimension and conformation of the grafted polymers. Assuming a freely-jointed chain model, the radius of gyration ($\sqrt{< R_g^2 >}$) of the grafted PMMA with molecular weight of 158 kDa was calculated to be 10.15 nm using $< R_g^2 >= \frac{N_0 b^2}{6} = \frac{\frac{158{,}000}{M_0} b^2}{6}$, where Kuhn length (b) and molar mass of Kuhn segment (M_0) were 1.53 nm and 598 g/mol for PMMA, respectively, and number of Kuhn segment (N_0) was calculated as polymer molar mass divided by M_0.[50, 63] Additionally, given the grafting density of 0.18 chains/nm^2, we calculated the chain-to-chain distance (D) to be 2.36 nm ($\sqrt{\frac{1\ chain}{0.18\ chains/nm^2}}$). Since $<R_g>$ is greater than D, we assume that the grafted polymers are in a moderate-density regime where adjacent chains can entangle with each other (**Figure 6c insets**). Therefore, the polymerization process decelerated and deviated from first order reaction at later stage due to the chain entanglement and steric hindrance, which enveloped the propagating chain front and impeded the polymerization. In fact, further increasing polymerization time beyond 6 h did not significantly increase molecular weight nor monomer conversion. As indicated by Kumar et al., investigating the two empirical parameters $\sigma \cdot \sqrt{N}$ and $\frac{P}{N}$, where P and N were degree of polymerization of matrix chain and grafted chain, respectively, is a useful quantitative measurement for defining the particle-matrix interaction in a polymer composite. For our composite system, we found out that $\sigma \cdot \sqrt{N} = 7.16$ and $\frac{P}{N} = 0.76$ with the matrix polymer molecular weight being 120 kDa. Our results fall into the well-dispersion regime for a polymer composite system, indicating a strong particle-matrix interaction.

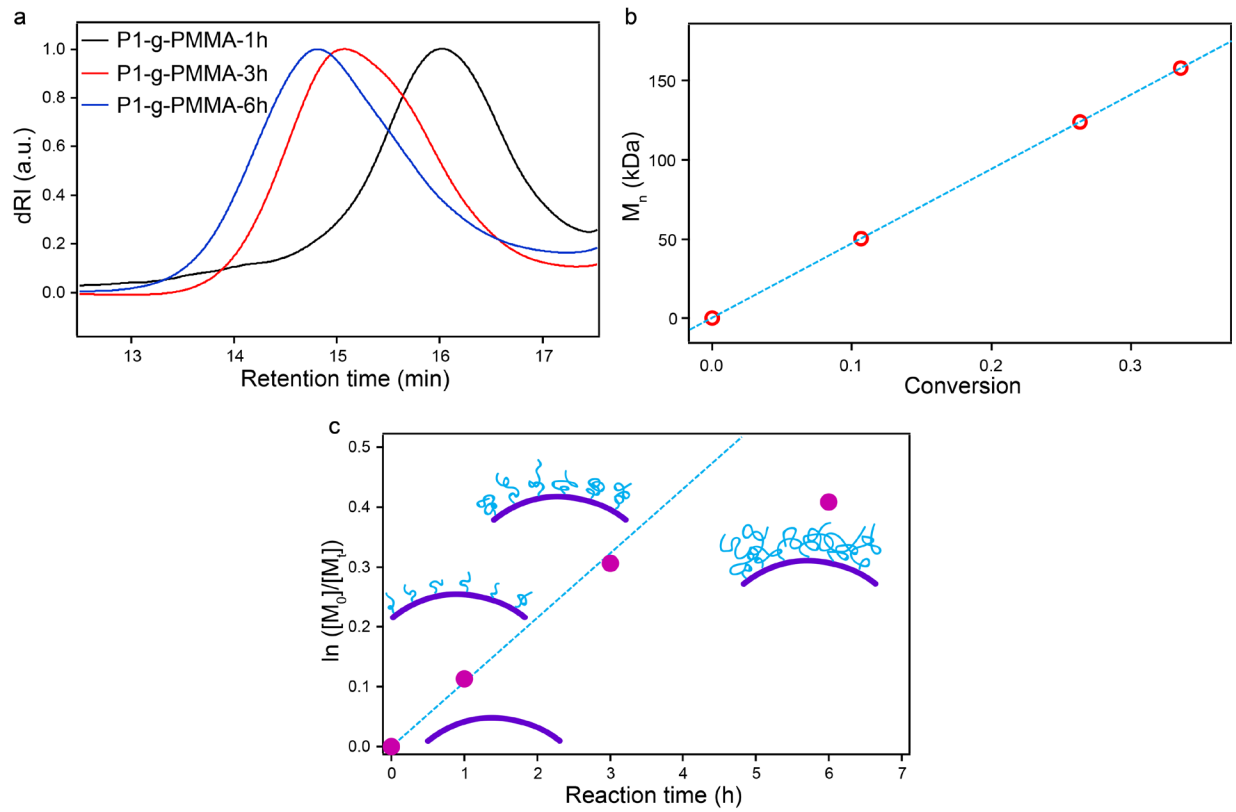

Figure 6. (a) SEC traces of P1-g-PMMA at different polymerization times. SEC experiments were carried out in THF at 30 C using differential refractive index and multi-angle light scattering instruments. Differential refractive index signals are displayed. (b) M_n as a function of monomer conversion. (c) Kinetic study of the SI-ATRP process.

Table 1. Number average molecular weight, M_n, and molecular weight dispersity, Đ, of grafted PMMA at different polymerization time.

	M_n (kDa)	***Đ***
1h PZN	**50.3**	**1.14**
3h PZN	**124**	**1.31**
6h PZN	**158**	**1.34**

We investigated the effect of grafted polymer with different molecular weight on the mechanical properties of MOF-polymer composite. All samples were prepared to ensure the same aspect ratio (AR) of PCN-222. P2 and P3-MA denoted pristine PCN-222 with AR of 32 ± 9 and myristic acid (MA) functionalized PCN-222 with AR of 31 ± 6, respectively (Figure S8 and S9, Table S2). P3-MA was selected as a control since it was developed our previous work.[40] The Young's modulus and strength of these MOF-polymer composites were obtained from DMA tensile measurements (**Figure 7**). Pristine P2 and P3-MA displayed similar average moduli of 2.46 ± 0.29 and 2.43 ± 0.32 GPa, respectively, which are higher than that of PMMA (1.92 ± 0.27) and in good agreement with our previous publication. The comparable performance of P2 and P3-MA indicated that short alkyl chain functionalization was not sufficient to positively impact interfacial interactions and provide significant difference for mechanical reinforcement. In contrast, all the PMMA-grafted P1 samples exhibited prominent reinforcement compared to the controls. Increased molecular weight resulted in an increased average Young's modulus with values of 3.45 ± 0.29, to 3.92 ± 0.47 and 4.11 ± 0.31 GPa, for 50.3, 124, and 158 kDa, respectively. The strength of the samples, which measured the maximum stress before breaking, followed a similar trend as the Young's modulus (**Figure 7b**). According to previous literature, when the graft molecular weight is close or higher than matrix molecular weight, the particle dispersion and overall performance would be improved compared to low graft molecular weight.[42] As the graft molecular weight decreases, the matrix chains would no longer form chain entanglement with grafted polymers but deviate from the particle surface, resulting in voids and weak interface. In our case, the matrix molecular weight is 120 kDa and therefore, 124 kDa and 158 kDa grafts presented better mechanical reinforcement comparing to 50.3 kDa graft thorough the stronger interfacial polymer entanglement. With 158 kDa PMMA grafts, our highest reinforcement was determined to be a 114% increase in Young's modulus with respect to pure PMMA. In our previous work, we achieved a similar reinforcement level using non-grafted PCN-222 with AR of 54, which was nearly two-fold of the AR of P1-g-PMMA. In this work, the grafted high molecular weight polymers on MOF surface are capable of enhancing the mechanical properties despite of lower MOF AR. It is reasonable to hypothesize that if one could obtain both high particle AR and

strong particle-polymer interaction (e.g., high grafting molecular weight and grafting density), better mechanical reinforcement would be realized. Nonetheless, our composite system presented one of the highest mechanical reinforcing performances for MOF-polymer composite at such low MOF loading, thanks to the high AR and engineered interface.

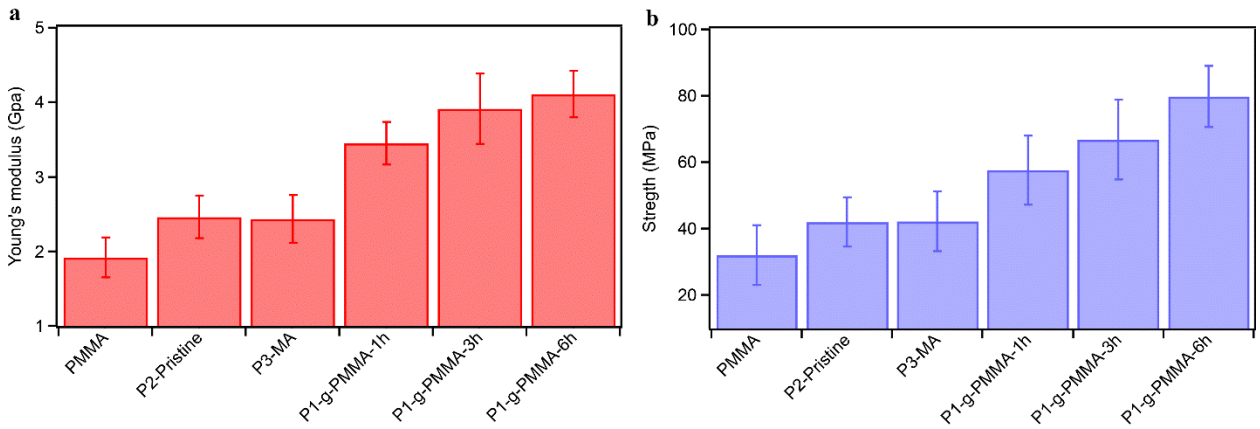

Figure 7. Young's modulus (a) and strength (b) of different MOF-polymer composites at 0.5 wt% MOF loading.

CONCLUSION

In this study, we developed a modified grafting-from strategy to systematically control the growth of PMMA on the surface of PCN-222 and investigated the relationship between surface-grafted polymers and composite mechanical properties. The successful SI-ATRP process was confirmed by exhaustive characterizations. The combination of ^{1}H-NMR and FTIR on P1-g-PMMA revealed the characteristic chemical moieties of PMMA. BET surface area analysis showed a drastic decrease of overall surface area but a consistent pore size distribution after grafting-from, indicating external surface pore blockage by the growth of polymer. Grafting density of P1-g-PMMA was calculated to be 0.18 chains/nm^2 based on TGA results. The molecular weight of grafted polymers ranged from 50.3 kDa to 158 kDa, which was facilely controlled by polymerization time. The correlation of polymer molecular weight and composite mechanical properties was revealed by DMA, which showcased an increase of both Young's modulus and strength with respect to grafting chain length. The highest modulus increment compared to pristine PMMA films was found to be 114% for 158 kDa grafting polymers with the MOF AR of 27. We

hypothesize that simultaneously achieving a high AR and an improved particle-matrix interface could afford a much stronger mechanical reinforcement, for which we are currently exploring.

ASSOCIATED CONTENT

Supporting Information

The following files are available free of charge.

NMR of initiator, table of reagents, calculation of initiator loading, reaction scheme of TCPP metalation, characterization of metalated TCPP, SEM of control P1-Ini-Zn and P1-g-PMMA, calculation of surface node density, SEM of various PCN-222, AR of various PCN-222. (word)

AUTHOR INFORMATION

Corresponding Authors

*Amanda J. Morris- Department of Chemistry and Macromolecules Innovation Institute, Virginia Tech, Blacksburg, Virginia 24060, United States; orcid.org/0000-0002-3512-0366; Email: ajmorris@vt.edu

Author Contributions

The manuscript was written through contributions of all authors. All authors have given approval to the final version of the manuscript.

ACKNOWLEDGMENT

This work was supported by National Science Foundation under Grant No. DMR-2109934. The electron microscopy was performed at the Nanoscale Characterization and Fabrication Laboratory, which is funded by the Virginia Tech National Center for Earth and Environmental Nanotechnology Infrastructure (NanoEarth), a member of the National Nanotechnology Coordinated Infrastructure (NNCI), supported by NSF (ECCS 1542100 and ECCS 2025151). The authors also thank Prof. John Matson for insightful discussion.

REFERENCES

1. Kalaj, M.; Bentz, K. C.; Ayala Jr, S.; Palomba, J. M.; Barcus, K. S.; Katayama, Y.; Cohen, S. M., MOF-polymer hybrid materials: From simple composites to tailored architectures. *Chem. Rev.* **2020,** *120* (16), 8267-8302.

2. Kitao, T.; Zhang, Y.; Kitagawa, S.; Wang, B.; Uemura, T., Hybridization of MOFs and polymers. *Chem. Soc. Rev.* **2017,** *46* (11), 3108-3133.

3. Lin, R.; Hernandez, B. V.; Ge, L.; Zhu, Z., Metal organic framework based mixed matrix membranes: An overview on filler/polymer interfaces. *J. Mater. Chem. A* **2018,** *6* (2), 293-312.

4. Schmidt, B. V., Metal-organic frameworks in polymer science: polymerization catalysis, polymerization environment, and hybrid materials. *Macromol. Rapid Commun.* **2020,** *41* (1), 1900333.

5. Yang, S.; Karve, V. V.; Justin, A.; Kochetygov, I.; Espin, J.; Asgari, M.; Trukhina, O.; Sun, D. T.; Peng, L.; Queen, W. L., Enhancing MOF performance through the introduction of polymer guests. *Coord. Chem. Rev.* **2021,** *427*, 213525.

6. Zhang, Y.; Feng, X.; Yuan, S.; Zhou, J.; Wang, B., Challenges and recent advances in MOF–polymer composite membranes for gas separation. *Inorg. Chem. Front.* **2016,** *3* (7), 896-909.

7. Cao, L.; Tao, K.; Huang, A.; Kong, C.; Chen, L., A highly permeable mixed matrix membrane containing CAU-1-NH 2 for H 2 and CO 2 separation. *Chem. Comm.* **2013,** *49* (76), 8513-8515.

8. Zhang, R.; Ji, S.; Wang, N.; Wang, L.; Zhang, G.; Li, J. R., Coordination-driven in situ self-assembly strategy for the preparation of metal–organic framework hybrid membranes. *Angew. Chem., Int. Ed.* **2014,** *53* (37), 9775-9779.

9. Adatoz, E.; Avci, A. K.; Keskin, S., Opportunities and challenges of MOF-based membranes in gas separations. *Sep. Purif. Technol.* **2015,** *152*, 207-237.

10. Rodenas, T.; Luz, I.; Prieto, G.; Seoane, B.; Miro, H.; Corma, A.; Kapteijn, F.; Llabrés i Xamena, F. X.; Gascon, J., Metal–organic framework nanosheets in polymer composite materials for gas separation. *Nat. Mater.* **2015,** *14* (1), 48-55.

11. Zhao, J.; Losego, M. D.; Lemaire, P. C.; Williams, P. S.; Gong, B.; Atanasov, S. E.; Blevins, T. M.; Oldham, C. J.; Walls, H. J.; Shepherd, S. D., Highly Adsorptive, MOF-Functionalized Nonwoven Fiber Mats for Hazardous Gas Capture Enabled by Atomic Layer Deposition. *Adv. Mater. Interfaces* **2014,** *1* (4), 1400040.

12. Zhao, J.; Lee, D. T.; Yaga, R. W.; Hall, M. G.; Barton, H. F.; Woodward, I. R.; Oldham, C. J.; Walls, H. J.; Peterson, G. W.; Parsons, G. N., Ultra-fast degradation of chemical warfare agents using MOF–nanofiber kebabs. *Angew. Chem., Int. Ed.* **2016,** *128* (42), 13418-13422.

13. Lee, D. T.; Zhao, J.; Oldham, C. J.; Peterson, G. W.; Parsons, G. N., UiO-66-NH2 metal–organic framework (MOF) nucleation on TiO2, ZnO, and Al2O3 atomic layer deposition-treated polymer fibers: role of metal oxide on MOF growth and catalytic hydrolysis of chemical warfare agent simulants. *ACS Appl. Mater. Interfaces* **2017,** *9* (51), 44847-44855.

14. Lee, D. T.; Zhao, J.; Peterson, G. W.; Parsons, G. N., Catalytic "MOF-Cloth" formed via directed supramolecular assembly of UiO-66-NH2 crystals on atomic layer deposition-coated textiles for rapid degradation of chemical warfare agent simulants. *Chem. Mater.* **2017,** *29* (11), 4894-4903.

15. Barton, H. F.; Davis, A. K.; Lee, D. T.; Parsons, G. N., Solvothermal synthesis of MIL-96 and UiO-66-NH2 on atomic layer deposited metal oxide coatings on fiber mats. *JoVE* **2018,** (136), e57734.

16. Lemaire, P. C.; Zhao, J.; Williams, P. S.; Walls, H. J.; Shepherd, S. D.; Losego, M. D.; Peterson, G. W.; Parsons, G. N., Copper benzenetricarboxylate metal–organic framework nucleation mechanisms on metal oxide powders and thin films formed by atomic layer deposition. *ACS Appl. Mater. Interfaces* **2016,** *8* (14), 9514-9522.

17. Lee, D. T.; Jamir, J. D.; Peterson, G. W.; Parsons, G. N., Water-Stable Chemical-Protective Textiles via Euhedral Surface-Oriented 2D Cu–TCPP Metal-Organic Frameworks. *Small* **2019,** *15* (10), 1805133.

18. DeCoste, J. B.; Denny Jr, M. S.; Peterson, G. W.; Mahle, J. J.; Cohen, S. M., Enhanced aging properties of HKUST-1 in hydrophobic mixed-matrix membranes for ammonia adsorption. *Chem. Sci.* **2016,** *7* (4), 2711-2716.

19. Peterson, G. W.; Browe, M. A.; Durke, E. M.; Epps III, T. H., Flexible SIS/HKUST-1 mixed matrix composites as protective barriers against chemical warfare agent simulants. *ACS Appl. Mater. Interfaces* **2018,** *10* (49), 43080-43087.

20. Peterson, G. W.; Lu, A. X.; Hall, M. G.; Browe, M. A.; Tovar, T.; Epps III, T. H., MOFwich: sandwiched metal–organic framework-containing mixed matrix composites for chemical warfare agent removal. *ACS Appl. Mater. Interfaces* **2018,** *10* (8), 6820-6824.

21. Zhang, X.; Zhang, Q.; Yue, D.; Zhang, J.; Wang, J.; Li, B.; Yang, Y.; Cui, Y.; Qian, G., Flexible Metal–Organic Framework-Based Mixed-Matrix Membranes: A New Platform for H2S Sensors. *Small* **2018,** *14* (37), 1801563.

22. Peterson, G. W.; Lu, A. X.; Epps III, T. H., Tuning the morphology and activity of electrospun polystyrene/UiO-66-NH2 metal–organic framework composites to enhance chemical warfare agent removal. *ACS Appl. Mater. Interfaces* **2017,** *9* (37), 32248-32254.

23. McCarthy, D. L.; Liu, J.; Dwyer, D. B.; Troiano, J. L.; Boyer, S. M.; DeCoste, J. B.; Bernier, W. E.; Jones Jr, W. E., Electrospun metal–organic framework polymer composites for the catalytic degradation of methyl paraoxon. *New J. Chem.* **2017,** *41* (17), 8748-8753.

24. López-Maya, E.; Montoro, C.; Rodríguez-Albelo, L. M.; Aznar Cervantes, S. D.; Lozano-Pérez, A. A.; Cenís, J. L.; Barea, E.; Navarro, J. A., Textile/Metal–Organic-Framework Composites as Self-Detoxifying Filters for Chemical-Warfare Agents. *Angew. Chem., Int. Ed.* **2015,** *54* (23), 6790-6794.

25. Liang, H.; Yao, A.; Jiao, X.; Li, C.; Chen, D., Fast and sustained degradation of chemical warfare agent simulants using flexible self-supported metal–organic framework filters. *ACS Appl. Mater. Interfaces* **2018,** *10* (24), 20396-20403.

26. Yao, A.; Jiao, X.; Chen, D.; Li, C., Photothermally enhanced detoxification of chemical warfare agent simulants using bioinspired core–shell dopamine–melanin@ metal–organic frameworks and their fabrics. *ACS Appl. Mater. Interfaces* **2019,** *11* (8), 7927-7935.

27. Dwyer, D. B.; Dugan, N.; Hoffman, N.; Cooke, D. J.; Hall, M. G.; Tovar, T. M.; Bernier, W. E.; DeCoste, J.; Pomerantz, N. L.; Jones Jr, W. E., Chemical protective textiles of UiO-66-integrated PVDF composite fibers with rapid heterogeneous decontamination of toxic organophosphates. *ACS Appl. Mater. Interfaces* **2018,** *10* (40), 34585-34591.

28. Ortiz, A. U.; Boutin, A.; Fuchs, A. H.; Coudert, F.-X., Anisotropic Elastic Properties of Flexible Metal-Organic Frameworks: How Soft are Soft Porous Crystals? *Phys. Rev. Lett.* **2012,** *109* (19), 195502.

29. Morris, W.; Volosskiy, B.; Demir, S.; Gándara, F.; McGrier, P. L.; Furukawa, H.; Cascio, D.; Stoddart, J. F.; Yaghi, O. M., Synthesis, structure, and metalation of two new highly porous zirconium metal–organic frameworks. *Inorg. Chem.* **2012,** *51* (12), 6443-6445.

30. Mondol, N. H.; Jahren, J.; Bjørlykke, K.; Brevik, I., Elastic properties of clay minerals. *The Leading Edge* **2008,** *27* (6), 758-770.

31. Eichhorn, S. J.; Dufresne, A.; Aranguren, M.; Marcovich, N.; Capadona, J.; Rowan, S. J.; Weder, C.; Thielemans, W.; Roman, M.; Renneckar, S., Current international research into cellulose nanofibres and nanocomposites. *J. Mater. Sci.* **2010,** *45*, 1-33.

32. Šturcová, A.; Davies, G. R.; Eichhorn, S. J., Elastic modulus and stress-transfer properties of tunicate cellulose whiskers. *Biomacromolecules* **2005,** *6* (2), 1055-1061.

33. Li, H.; Tuo, L.; Yang, K.; Jeong, H.-K.; Dai, Y.; He, G.; Zhao, W., Simultaneous enhancement of mechanical properties and CO2 selectivity of ZIF-8 mixed matrix membranes: Interfacial toughening effect of ionic liquid. *J. Membr. Sci.* **2016,** *511*, 130-142.

34. Dai, X.; Cao, Y.; Shi, X.; Wang, X., Non-isothermal crystallization kinetics, thermal degradation behavior and mechanical properties of poly(lactic acid)/MOF composites prepared by melt-blending methods. *RSC Adv.* **2016,** *6* (75), 71461-71471.

35. Mahdi, E. M.; Tan, J.-C., Dynamic molecular interactions between polyurethane and ZIF-8 in a polymer-MOF nanocomposite: Microstructural, thermo-mechanical and viscoelastic effects. *Polymer* **2016,** *97*, 31-43.

36. Palomba, J. M.; Wirth, D. M.; Kim, J. Y.; Kalaj, M.; Clarke, E. M.; Peterson, G. W.; Pokorski, J. K.; Cohen, S. M., Strong, Ductile MOF–Poly(urethane urea) Composites. *Chem. Mater.* **2021,** *33* (9), 3164-3171.

37. Liu, C.; Feng, S.; Zhu, Z.; Chen, Q.; Noh, K.; Kotaki, M.; Sue, H.-J., Manipulation of Fracture Behavior of Poly(methyl methacrylate) Nanocomposites by Interfacial Design of a Metal–Organic-Framework Nanoparticle Toughener. *Langmuir* **2020,** *36* (40), 11938-11947.

38. Mondal, P.; Cohen, S. M., Self-healing mixed matrix membranes containing metal–organic frameworks. *Chem. Sci.* **2022,** *13* (41), 12127-12135.

39. Wang, H.; He, S.; Qin, X.; Li, C.; Li, T., Interfacial Engineering in Metal–Organic Framework-Based Mixed Matrix Membranes Using Covalently Grafted Polyimide Brushes. *J. Am. Chem. Soc.* **2018,** *140* (49), 17203-17210.

40. Yang, X.; Bonnett, B. L.; Spiering, G. A.; Cornell, H. D.; Gibbons, B. J.; Moore, R. B.; Foster, E. J.; Morris, A. J., Understanding the Mechanical Reinforcement of Metal–Organic Framework–Polymer Composites: The Effect of Aspect Ratio. *ACS Appl. Mater. Interfaces* **2021,** *13* (44), 51894-51905.

41. Borukhov, I.; Leibler, L., Enthalpic stabilization of brush-coated particles in a polymer melt. *Macromolecules* **2002,** *35* (13), 5171-5182.

42. Kumar, S. K.; Jouault, N.; Benicewicz, B.; Neely, T., Nanocomposites with polymer grafted nanoparticles. *Macromolecules* **2013,** *46* (9), 3199-3214.

43. Ash, B. J.; Schadler, L. S.; Siegel, R. W., Glass transition behavior of alumina/polymethylmethacrylate nanocomposites. *Mater. Lett.* **2002,** *55* (1), 83-87.

44. Ash, B. J.; Siegel, R. W.; Schadler, L. S., Glass-transition temperature behavior of alumina/PMMA nanocomposites. *J. Polym. Sci., Part B: Polym. Phys.* **2004,** *42* (23), 4371-4383.

45. Bansal, A.; Yang, H.; Li, C.; Benicewicz, B. C.; Kumar, S. K.; Schadler, L. S., Controlling the thermomechanical properties of polymer nanocomposites by tailoring the polymer–particle interface. *J. Polym. Sci., Part B: Polym. Phys.* **2006,** *44* (20), 2944-2950.

46. Hwang, G. L.; Shieh, Y. T.; Hwang, K. C., Efficient load transfer to polymer-grafted multiwalled carbon nanotubes in polymer composites. *Adv. Funct. Mater.* **2004,** *14* (5), 487-491.

47. Bonnett, B. L.; Ilic, S.; Flint, K.; Cai, M.; Yang, X.; Cornell, H. D.; Taylor, A.; Morris, A. J., Mechanistic Investigations into and Control of Anisotropic Metal–Organic Framework Growth. *Inorg. Chem.* **2021,** *60* (14), 10439-10450.

48. Yang, S.; Hu, W.; Nyakuchena, J.; Fiankor, C.; Liu, C.; Kinigstein, E. D.; Zhang, J.; Zhang, X.; Huang, J., Unravelling a long-lived ligand-to-metal cluster charge transfer state in Ce–TCPP metal organic frameworks. *Chem. Comm.* **2020,** *56* (90), 13971-13974.

49. Sugnaux, C.; Lavanant, L.; Klok, H.-A., Aqueous Fabrication of pH-Gated, Polymer-Brush-Modified Alumina Hybrid Membranes. *Langmuir* **2013,** *29* (24), 7325-7333.

50. Brandrup, J.; Immergut, E. H.; Grulke, E. A.; Abe, A.; Bloch, D. R., *Polymer Handbook (4th edition)*. John Wiley & Sons: 1999; Vol. 89; pp 571.

51. Zdyrko, B.; Luzinov, I., Polymer brushes by the “grafting to” method. *Macromol. Rapid Commun.* **2011,** *32* (12), 859-869.

52. Zoppe, J. O.; Ataman, N. C.; Mocny, P.; Wang, J.; Moraes, J.; Klok, H.-A., Surface-initiated controlled radical polymerization: state-of-the-art, opportunities, and challenges in surface and interface engineering with polymer brushes. *Chem. Rev.* **2017,** *117* (3), 1105-1318.

53. Feng, X.-T.; Yu, J.-G.; Lei, M.; Fang, W.-H.; Liu, S., Toward understanding metal-binding specificity of porphyrin: a conceptual density functional theory study. *J. Phys. Chem. B* **2009,** *113* (40), 13381-13389.

54. Cherian, S.; Wamser, C. C., Adsorption and Photoactivity of Tetra(4-carboxyphenyl)porphyrin (TCPP) on Nanoparticulate TiO2. *J. Phys. Chem. B* **2000,** *104* (15), 3624-3629.

55. Shaikh, Shaunak M.; Chakraborty, A.; Alatis, J.; Cai, M.; Danilov, E.; Morris, A. J., Light harvesting and energy transfer in a porphyrin-based metal organic framework. *Faraday Discuss.* **2019,** *216* (0), 174-190.

56. Krol, P.; Chmielarz, P., Recent advances in ATRP methods in relation to the synthesis of copolymer coating materials. *Prog. Org. Coat.* **2014,** *77* (5), 913-948.

57. Balke, S.; Hamielec, A., Bulk polymerization of methyl methacrylate. *J. Appl. Polym. Sci.* **1973,** *17* (3), 905-949.

58. Park, S. J.; Cho, M. S.; Lim, S. T.; Choi, H. J.; Jhon, M. S., Synthesis and dispersion characteristics of multi-walled carbon nanotube composites with poly (methyl methacrylate) prepared by in-situ bulk polymerization. *Macromol. Rapid Commun.* **2003,** *24* (18), 1070-1073.

59. Feng, D.; Gu, Z. Y.; Li, J. R.; Jiang, H. L.; Wei, Z.; Zhou, H. C., Zirconium-metalloporphyrin PCN-222: mesoporous metal–organic frameworks with ultrahigh stability as biomimetic catalysts. *Angew. Chem., Int. Ed.* **2012,** *124* (41), 10453-10456.

60. Maillard, D.; Kumar, S. K.; Fragneaud, B.; Kysar, J. W.; Rungta, A.; Benicewicz, B. C.; Deng, H.; Brinson, L. C.; Douglas, J. F., Mechanical properties of thin glassy polymer films filled with spherical polymer-grafted nanoparticles. *Nano Lett.* **2012,** *12* (8), 3909-3914.

61. Matyjaszewski, K.; Patten, T. E.; Xia, J., Controlled/“living” radical polymerization. Kinetics of the homogeneous atom transfer radical polymerization of styrene. *J. Am. Chem. Soc.* **1997,** *119* (4), 674-680.

62. Goto, A.; Fukuda, T., Kinetics of living radical polymerization. *Progress in Polymer Science* **2004,** *29* (4), 329-385.

63. Mark, J. E., *Physical properties of polymers handbook*. Springer: 2007; Vol. 1076; pp 450.

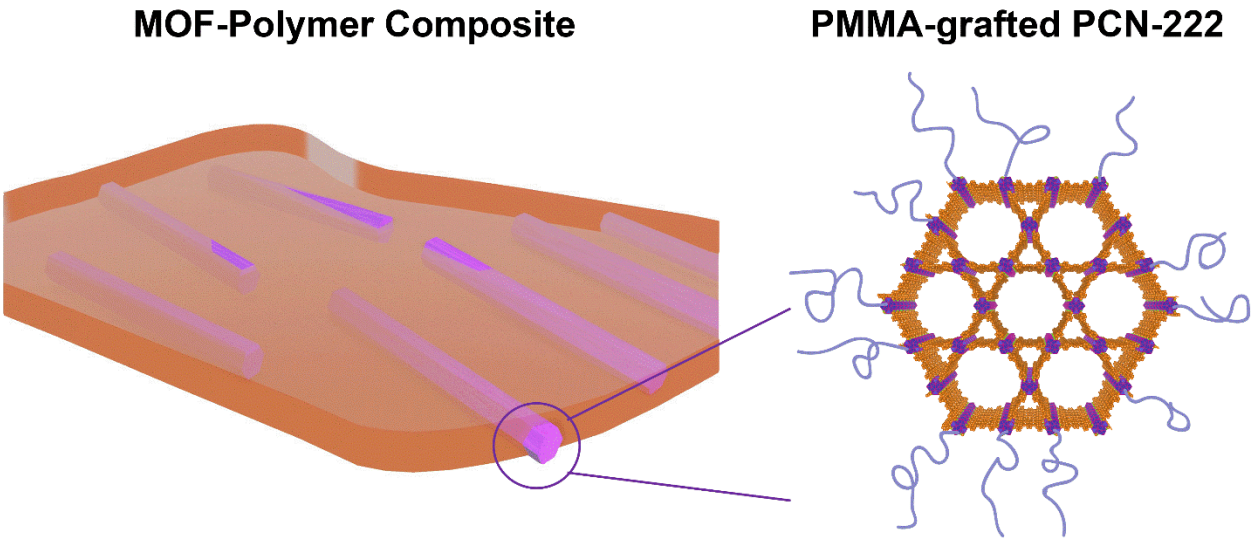
MOF-Polymer Composite
PMMA-grafted PCN-222

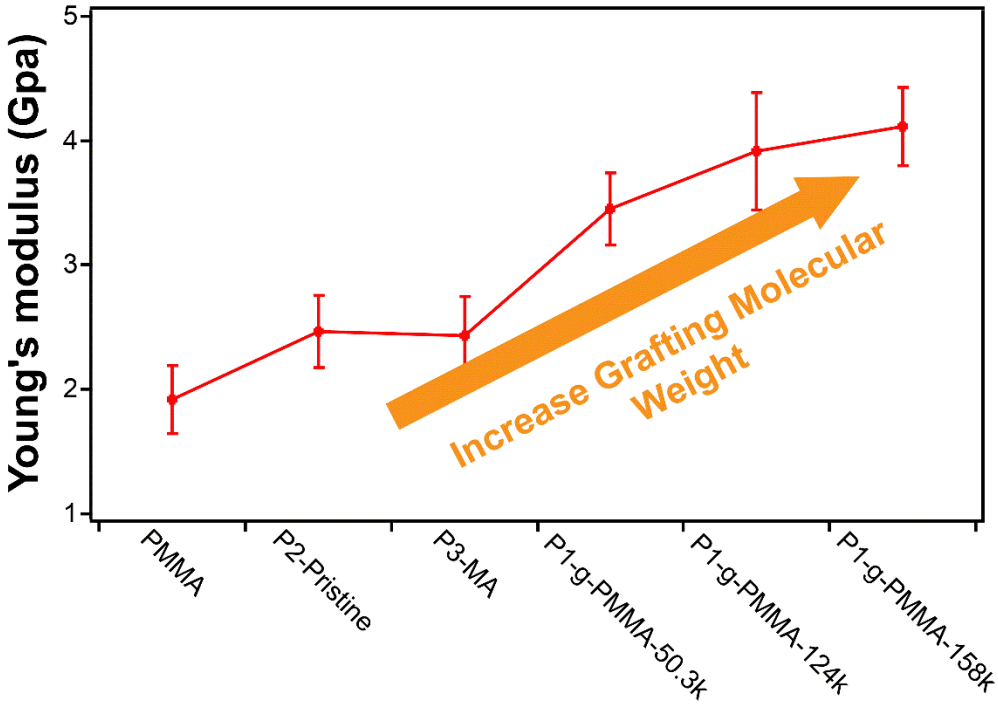
Young's modulus (Gpa)
5
4
3
2
1
Increase Grafting Molecular Weight
PMMA
P2-Pristine
P3-MA
P1-g-PMMA-50.3k
P1-g-PMMA-124k
P1-g-PMMA-158k